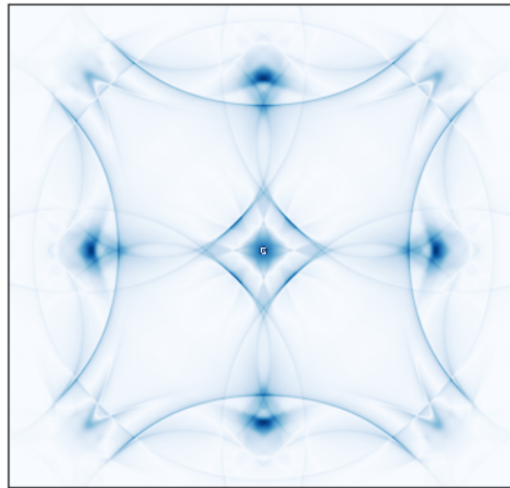




---

# Quasi-particle Interference in overdoped Cuprates

---



THESIS

submitted in partial fulfillment of the  
requirements for the degree of

MASTER OF SCIENCE

in

PHYSICS

Author :	A.H.W.M. Nieuwesteeg
Student ID :	s1536923
Supervisor :	Prof. Dr. K. E. Schalm
2 <sup>nd</sup> corrector :	Dr. M. P. Allan

Leiden, The Netherlands, August 25, 2021



# Quasi-particle Interference in overdoped Cuprates

A.H.W.M. Nieuwesteeg

Huygens-Kamerlingh Onnes Laboratory, Leiden University  
P.O. Box 9500, 2300 RA Leiden, The Netherlands

August 25, 2021

## Abstract

The advent of high-temperature superconductivity in 1986 [1] shook the foundations of superconductivity. First identified in the cuprate  $\text{Ba}_n\text{La}_{5-n}\text{Cu}_5\text{O}_{5+x}$ , it propelled these elusive materials unto the center stage of physics. To let the cuprates divulge their secrets, quasi-particle interference is nowadays an indispensable tool. In the nascent days of the field research using this method primarily has been performed on the underdoped version of the cuprates. The overdoped regime however is less intensively studied. In this study we apply the T-matrix method to model QPI in the overdoped phase. We modify a simulation for underdoped cuprates to make it suitable for application on the desired regime. Then, in order to obtain a quantitative analysis of our result we compare experiment and simulation using the Structural Similarity Index Measure. Using this method the filling of the gap, the characteristics of the dispersion bands and the van Hove singularity are investigated.



# Contents

<b>1</b>	<b>Introduction</b>	<b>1</b>
<b>2</b>	<b>Theory</b>	<b>3</b>
2.1	Cuprates	3
2.1.1	D-wave superconductivity	5
2.2	Quasi-particle Interference	8
2.2.1	The octet-model	9
2.2.2	The appropriate size of q-space	10
<b>3</b>	<b>Modelling the scattering</b>	<b>13</b>
3.1	Tight-binding model	13
3.2	Autocorrelation	15
3.3	T-matrix method	16
3.3.1	The effect of the potential	19
3.4	Adressing non-periodicity in q-space	20
<b>4</b>	<b>Results</b>	<b>23</b>
4.1	Breaking of periodicity in q-space	23
4.2	Filling the gap	25
4.3	Adding holes	25
4.4	The van Hove singularity	27
<b>5</b>	<b>Discussion</b>	<b>33</b>
5.1	The periodicity of q-space	33
5.2	Including holes in the model	34
5.3	Setting the gap to zero	35
5.4	Final remarks	35
<b>6</b>	<b>Conclusion and outlook</b>	<b>37</b>

<b>Appendices</b>	<b>47</b>
<b>A Comparing images using the SSIM</b>	<b>47</b>
<b>B Images for mentioned parameters</b>	<b>49</b>

# Introduction

"By straight Fourier analysis I found to my delight that the wave differed from the plane wave of free electrons only by a periodic modulation." This quote is attributed to Felix Bloch, spoken after he had invented the eponymous Bloch wave. While the Bloch wave is delightful to him, to experimental physicists using a scanning tunneling microscope (STM) it is rather uninteresting. The point is that from a plane Bloch wave no information about the local electronic properties of a material can be obtained. For example, an STM scanning a perfect metal, in which electrons behave like Bloch waves, simply sees a flat surface.

To our delight not every physical system is described by a perfect Bloch wave. As calculated by Friedel [2] impurities in the lattice cause ripples in the flat electronic surface. These so-called Friedel oscillations can actually be observed. Furthermore, any non-periodic potential would break up the plane Bloch waves and reveal the enigmatic electronic properties of the material. The first application of this principle to cuprates was by Hoffman [3]. Using Fourier transformed STM data she managed to image the pattern resulting from the interference of the Bloch waves. This interference did not result from ordinary electrons, but existed because of Bogoliubov quasi-particles. These quasi-particles are broken Cooper pairs, existing in the superconducting phase. With the advent of a theoretical explanation for the scattering by Wang [4] the use of quasi-particle interference (QPI) to study cuprates was a resounding success. The theory invoked to explain the experiment by Hoffman was the T-matrix calculation. Using Quantum Field Theory the scattering of quasi-particles against each other, using a single point-like impurity, was calculated. The main focus of their research was however on the underdoped cuprates.

This thesis will apply the T-matrix to QPI in the overdoped regime. Prin-

cipally a method is suggested to better simulate the non-periodicity of the QPI in experiments. Having obtained a suitable algorithm, real experimental data will be compared with the simulation in order to deduce physical characteristics of the overdoped cuprates. The dispersion relation of the Bogoliubov quasiparticle will be investigated, as well as the filling of the superconducting gap. Concludingly a search will be led into identifying the van Hove singularity in the experiments. All of this will not merely be performed by eye, but a measure to quantitatively analyse results shall be used. The Structural Similarity Index Measure will compare experiment to simulation, to vilify or sanctify the conclusions obtained by human analysis.

# Theory

The goal of this research is to match a model to measurements on overdoped cuprates. Hence this section starts with a general exposé about cuprates. Only the superconducting part of the phase diagram will be discussed in depth. The physical aspects of the other phases are either encapsulated in the interaction of the superconducting gap with the Fermi surface or not relevant. Next the physics behind quasi-particle interference is explained. Without this interference, reconstructing the Fermi-surface would be impossible, as the local density of states would not depend on the dispersion relation. Special emphasis will be placed on the difference between k-space and q-space.

## 2.1 Cuprates

Cuprates are layered perovskites. Hence they consist of at least two two-dimensional layers stacked on top of each other. These layers look repetitive in plane, but differ from each other out of plane. In plane the atoms are bounded by strong metallic bonds. However out of plane the layers are connected through van der Waals bonds. Therefore it is often relatively easy to separate the layers of these materials very cleanly. As an example the perovskite structure of  $\text{Bi}_2\text{Sr}_2\text{Ca}_1\text{Cu}_2\text{O}_{8+x}$  is shown in Fig 2.1.

In the case of the cuprates, the common denominator is that one layer is a copper oxide plane. The main conductivity happens in this plane. The other layers can be made of all kinds of exotic atoms. The cuprate to be modelled is  $\text{Bi}_2\text{Sr}_2\text{Ca}_{n-1}\text{Cu}_n\text{O}_{2n+4+x}$ . Here the  $n$  is an integer indicating that several different species of this material exist. Every increase of  $n$  gives additional planes and tweaks the characteristics of the material.

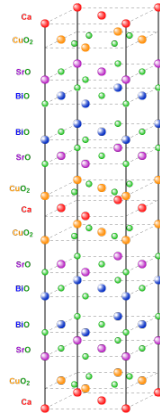


**Figure 2.1:** The perovskite structure of  $\text{Bi}_2\text{Sr}_2\text{Ca}_1\text{C}_1\text{O}_{6+x}$ . The unit cell has a size of  $5.4\text{\AA} \times 5.4\text{\AA}$ . Taken from Ref. [5]

Often the versions of  $\text{Bi}_2\text{Sr}_2\text{Ca}_{n-1}\text{Cu}_n\text{O}_{2n+4+x}$  are labelled by the nomenclature Bi-22(n-1)(n). The third number indicates the amount of calcium atoms, the fourth the amount of copper atoms. An example of the varying characteristics is the critical temperature  $T_c$ . This may range from roughly 33K for Bi-2201 up to 105K for Bi-2223 [6]. There is one other peculiarity of the cuprates, resembled by the  $x$  in the aforementioned formula. Namely, the copper oxide plane can be doped. This happens through the introduction of oxygen atoms. Generally this is done by annealing the formed BiSCCO in a high oxygen atmosphere. By adding oxygen atoms holes are introduced into the system. A somewhat simplified explanation for this is that oxygen has a higher electronegativity than copper. Therefore when introducing an oxygen atom, it tends to bind free electrons very tightly. This removal of the freedom of movement of an electron basically amounts to creating a hole. In order to fathom how this affects the cuprates, we take a concrete example. Looking at Fig. 2.2 we see the phase diagram of Bi-2212. Here the  $x$ -axis represents the amount of holes in the material, called the doping. By doping the compound the system moves through a plethora of phases. On the left side of the diagram the system is in the antiferromagnetic phase. Here the system behaves as an insulator. Completely to the right Bi-2212 is in a Fermi liquid regime and behaves like a conductor. An important doping level is the so called optimal doping. In the figure the optimal doping is indicated by the arrow with  $P_{c2}$ . Here the critical temperature is highest. To the left of the doping a cuprate is called underdoped. Right to the critical temperature the cuprate is called overdoped. As mentioned our main area of interest will be the overdoped region.

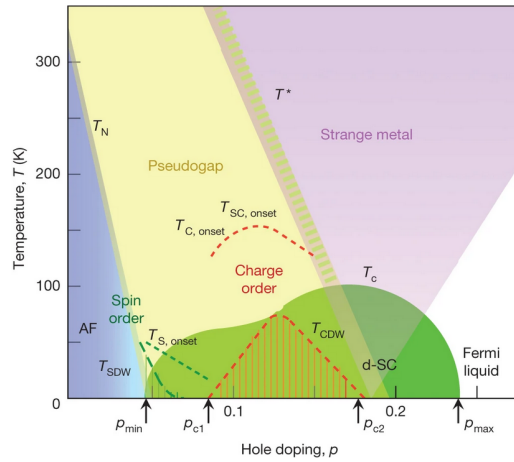


**Figure 2.2:** The phase diagram of Bi-2212, reprinted from Ref. [7].

### 2.1.1 D-wave superconductivity

The cuprates are a type-II superconductor. This means, that contrary to type-I superconductors, magnetic flux is capable of penetrating the material while it is superconducting. For an ordinary superconductor there is critical field  $H_c$  upon which superconductivity breaks down. Since for a type-II superconductor the magnetic flux can gradually penetrate, the supercurrent densities can be much higher. However, the magnetic flux penetration is not even the most fascinating part of the cuprate superconducting phase. To understand why cuprates are so special, first normal superconductivity needs some explanation. In an ordinary superconductor below a certain temperature, called the critical temperature ( $T_c$ ), electrons start to form so-called Cooper pairs. Because the electrons form these pairs and condense in a single wavefunction, a gap opens in the DOS at the Fermi energy. The opening of a gap means that there are no allowed electron states anymore with the gap energy. A sketch of the DOS for a conventional superconductor is given by the black line in Fig. 2.3. The size of the gap depends on the temperature (apart from material characteristics). The lower the temperature, the bigger the gap. Furthermore the size of the gap also indicates the difficulty of breaking the Cooper pairs and therefore the resilience of the superconductivity. The bigger the gap, the harder it is to break the superconductivity using a current or a magnetic field.

In contrast with s-wave superconductors, the cuprates are d-wave superconductors. This ephemeral quality was long uncertain, but it was conclusively shown by Tsuei et al. [8]. The characterisation of the type

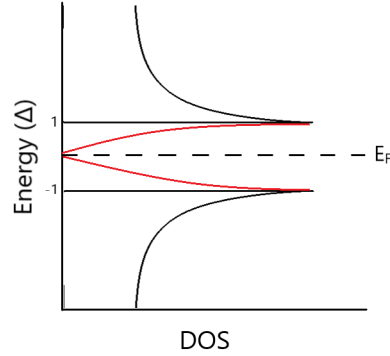


**Figure 2.3:** The black line resembles the *s*-wave superconductor with zero DOS within the gap. The red line indicates the additional filling of the gap by a *d*-wave superconductor.

of wave is similar to the terminology used for electron orbitals [9]. The Cooper pairs consist of two electrons. Just like electrons around nuclei, the combined electrons can have an angular momentum. This momentum is characterised by the same letters: *s*, *p*, *d*, *f*. Thus a *d*-wave means that the Cooper pair has a non-zero angular momentum. Importantly a *d*-wave superconductor has an anisotropic bandgap. The gap can be parametrised as

$$\Delta(\mathbf{k}) = \frac{\Delta_0}{2}(\cos(k_x) - \cos(k_y)) \quad (2.1)$$

Which results in a gap shown by Fig. 2.4. The direction where the gap is zero is generally designated as the nodal direction. The part where the gap is maximal is termed the antinode. In the figure the antinodes are deep-red and the nodes are shown in blue.

Obviously the anisotropic gap yields a non-zero density of states within the gap, contrary to *s*-wave superconductors. This effect is shown by the red line in 2.3.

The superconducting gap is both dependent on temperature and doping. General agreement stipulates that in the underdoped phase the gap increases with increased doping. However in the overdoped phase, the gap does not necessarily decrease with even further doping. According to research using ARPES [10] [11] the gap is more likely to fill, than to shrink. Looking at Fig. 2.3 a shrinking gap means that the peaks move closer together. Gap-filling would mean peaks at the same location, but an even further increase of density of states between them. This is rather odd. As mentioned, we expect the difficulty of breaking the superconducting state with the gap size. Therefore, a non-decreasing gap would suggest ongoing

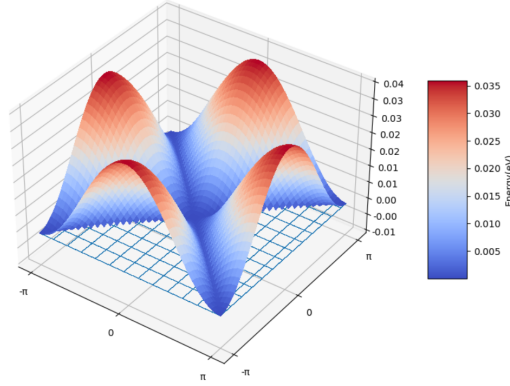


**Figure 2.4:** The anisotropic  $d$ -wave gap. The nodal direction is along the blue crevice, while the antinodes are given by the red tops. Observe how the gap is zero along the nodal direction.

superconductivity. However, at high doping the cuprates do stop superconducting, so apparently filling up the gap is sufficient to suppress it.

Finally a very important remark on the excitations around the superconducting gap is in place. Contrary to being electrons these excitations are Bogoliubov quasiparticles [12]. The excitations can be thought of as broken Cooper pairs. The Bogoliubovs are linear combinations of electrons and holes. The creation operators for the two spin directions are given by Eq. 2.3. In the linear combination  $a_k^{(\dagger)}$  gives the annihilation (creation) operator for an electron. Of course the annihilation of an electron equals the creation of a hole.

$$b_{k0}^\dagger = u_k^* a_{k\uparrow}^\dagger - v_k^* a_{-k\downarrow} \quad (2.2)$$

$$b_{k1}^\dagger = u_k^* a_{-k\downarrow}^\dagger + v_k^* a_{k\uparrow} \quad (2.3)$$

The coefficients of these relations have to obey

$$|v_k|^2 = 1 - |u_k|^2 = \frac{1}{2} \left(1 - \frac{\epsilon_k}{E_k}\right) \quad (2.4)$$

The dispersion relation of these quasiparticles is given by

$$E(\mathbf{k}) = \sqrt{\epsilon_k^2 + \Delta_k^2} \quad (2.5)$$

With  $\epsilon_k$  the dispersion relation of the normal particles and  $\Delta_k$  the size of the gap. The coefficients are clearly energy dependent. Therefore quasiparticles are turned back into normal particles at high energies relative to

the gap. When for example the gap is zero (and thus all energies are high compared to it),  $u_k^* = 1$  and  $v_k^* = 0$ . The creation of a quasi-particle is equal to creating an electron in that case. It is the quasi-particles resulting from Eq. 2.3 that interfere and thereby create the coveted anisotropic LDOS.

## 2.2 Quasi-particle Interference

In general when measuring the local density of states (LDOS) one expects it to be locally independent of the Fermi surface. The reason for this is the Bloch wavefunction. The Bloch wavefunction arises as an eigenfunction and hence solution to an periodic potential and is given by

$$\psi_{\mathbf{k}}(\mathbf{r}) = e^{i\mathbf{k}\cdot\mathbf{r}} u_{\mathbf{k}}(\mathbf{r}) \quad (2.6)$$

With  $u_{\mathbf{k}}(\mathbf{r})$  a function that is periodic with the lattice. Since the local density of states is defined by

$$g(E) \propto \sum_{\mathbf{k}} |\psi_{\mathbf{k}}(\mathbf{r})|^2 \delta(E - \epsilon(\mathbf{k})) \quad (2.7)$$

it is obvious that the LDOS is locally independent of  $\mathbf{k}$  in space, after substituting the Bloch wavefunction. When the Bloch wavefunction is multiplied by its complex conjugate the exponentials cancel. Therefore only the  $|u_{\mathbf{k}}(\mathbf{r})|^2$ -term remains. This term does only very weakly depend on  $\mathbf{k}$ , thus all spatial information regarding  $\mathbf{k}$  is lost. The remaining  $|u_{\mathbf{k}}(\mathbf{r})|^2$  is the source of the Bragg peaks and is often used to determine the rotation of the unit cell. In the case of the presence of impurities the aforementioned line of reasoning does not hold. Now the new eigenfunctions are linear combinations of the unperturbed Bloch wavefunctions. We may write the new Bloch wavefunction as:

$$\psi_{\mathbf{k}_1, \mathbf{k}_2}(\mathbf{r}) = c_1 e^{i\mathbf{k}_1 \cdot \mathbf{r}} u_{\mathbf{k}_1}(\mathbf{r}) + c_2 e^{i\mathbf{k}_2 \cdot \mathbf{r}} u_{\mathbf{k}_2}(\mathbf{r}) \quad (2.8)$$

Taking both  $u_{\mathbf{k}}(\mathbf{r})$ -terms as equal since we expect these waves to exist on the same lattice and therefore experience the same potential. Plugging this into Eq. 2.7 gives

$$g(E) \propto \sum_{\mathbf{k}_1} \sum_{\mathbf{k}_2} (c_1 c_2^* e^{i(\mathbf{k}_1 - \mathbf{k}_2) \cdot \mathbf{r}} |u_{\mathbf{k}_1}(\mathbf{r})|^2 + c_1^* c_2 e^{i(\mathbf{k}_2 - \mathbf{k}_1) \cdot \mathbf{r}} |u_{\mathbf{k}_2}(\mathbf{r})|^2 + |c_1 u_{\mathbf{k}_1}(\mathbf{r})|^2 + |c_2 u_{\mathbf{k}_2}(\mathbf{r})|^2) \delta(E - \epsilon(\mathbf{k}_1)) \delta(E - \epsilon(\mathbf{k}_2)) \quad (2.9)$$

Resulting in waves with a new wavevector  $\mathbf{q} = \mathbf{k}_1 - \mathbf{k}_2$ . For spatial variations dependent on  $\mathbf{q}$  there now exist a  $\mathbf{k}_1$  and  $\mathbf{k}_2$  that differ but for which the energy is equal, e.g.  $\epsilon(\mathbf{k}_1) = \epsilon(\mathbf{k}_2)$ . An one-dimensional quadratic dispersion relation yields a trivial example. if  $\epsilon = k^2$ , then  $\epsilon(\mathbf{k}) = \epsilon(-\mathbf{k})$  resulting in waves with  $\mathbf{q} = \pm 2\mathbf{k}$ . The next section will explain how these new waves results in comprehensible patterns.

### 2.2.1 The octet-model

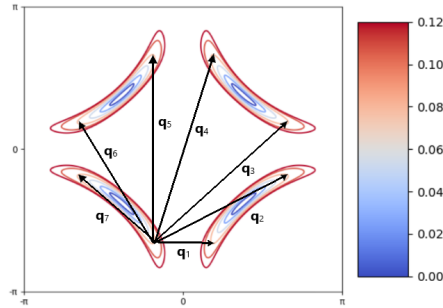
The octet model is used to qualitatively explain the QPI patterns seen in the underdoped cuprates. Though research was mainly concerned with overdoped cuprates, it is nevertheless insightfull to glean at this model to obtain a rough feeling for how QPI works. The generalisation to overdoped cuprates is straightforward. The scattering amplitude in a superconductor is given by [13]:

$$w(i \rightarrow f) \propto \frac{2\pi}{\hbar} (u_{k_i} u_{k_f} \pm v_{k_i} v_{k_f}) |V(\mathbf{q})|^2 g_i(E_i, \mathbf{k}_i) g_f(E_f, \mathbf{k}_f) \quad (2.10)$$

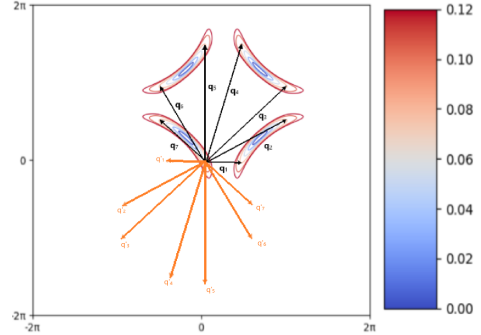
Here  $u_k$  and  $v_k$  are the same coefficients used in Eq. 2.3. As in Eq. 2.9  $g(E, \mathbf{k})$  gives the density of states at a given  $E$  and  $\mathbf{k}$ . From Eq. 2.10 it is clear that locations in  $\mathbf{k}$ -space with a high density of states overwhelmingly contribute to the scattering. Especially scattering from one location with a high DOS towards another location with a high DOS is pronounced. The question is now of course where these high DOS lie. This is where the octet model comes into play. The Fermi surface in the underdoped phase namely has pretty well defined loci of high DOS. In Fig. 2.5a such a surface is shown. Generally the axis for such a  $\mathbf{k}$ -space image run from  $-\frac{\pi}{a}$  to  $\frac{\pi}{a}$  with  $a$  the length of the unit cell. For convenience we set this  $a$  to unity in all further reference. Since the density of states is given by

$$g(E) \propto \frac{1}{\nabla_{\mathbf{k}} E_{\mathbf{k}}} \quad (2.11)$$

it is inverse to the steepness of the Fermi surface. At the tips of the banana-shaped forms the contour of constant energy (CCE) are relatively far apart. This means that the surface is quite flat, and hence at the tips of contours in Fig. 2.5a, the DOS is very high. In the octet model the approximation is that only these tips of the CCE contribute to the scattering, resulting in 8 distinctive scattering vectors. We note that the length of a vector  $\mathbf{q}$  only depends on the difference between  $\mathbf{k}_1$  and  $\mathbf{k}_2$ , not on their absolute location in  $\mathbf{k}$ -space. Hence all  $\mathbf{q}$ -vectors point outward from the



(a) Contours of constant energy. The closer the contours, the steeper the Fermi surface and the lower the density of states. The main scattering vectors are shown by the arrows.



(b) The scattering vectors of Fig 2.5a translated in to  $q$ -space. Observe how all vectors originate from the origin and that therefore  $q$ -space is twice as big as  $k$ -space.

point  $(0,0)$  in  $q$ -space. An important note is that due to this relocation at the origin,  $q$ -space is twice as big as  $k$ -space. If an inappropriately sized  $q$ -space is taken, the vectors that are too long are folded back into it. Also the scattering between two loci of high DOS works of course both ways. Therefore, as can be seen in Fig. 2.5b, every scattering vector also exists as minus itself. Because every point scatters to all others in reality the  $q$ -vectors are fourfold symmetric, for clarity this is not shown.

An interesting course of action is continuously increasing the energy and thereby extending the CCE's even further. In that case the Fermi surface at the tips of the CCE becomes flat. A flat surface means a gradient of zero and therefore Eq. 2.11 diverges. The location with a diverging DOS due to the flatness of the surface is called the van Hove singularity.

## 2.2.2 The appropriate size of $q$ -space

Briefly glanced over in the previous section, the appropriate size of  $q$ -space merits its own analysis. As mentioned  $q$ -space should be twice the size of  $k$ -space. In theoretical simulations however  $q$ -space is generally taken to be the same size as  $k$ -space. The reason for this is that for a perfectly periodic Fermi surface all  $q$ -vectors that differ by an integer multiple of  $2\pi$  in both  $q_x$  and  $q_y$  are physically equivalent. Therefore if a vector  $q_1$  lies outside the  $q$ -space from  $-\pi$  to  $\pi$  there is a  $q$ -vector  $q'_1 = q_1 \bmod 2\pi$  with exactly the same characteristics. Because most of the time QPI patterns are calculated using a tight-binding model, which assumes perfect periodicity,

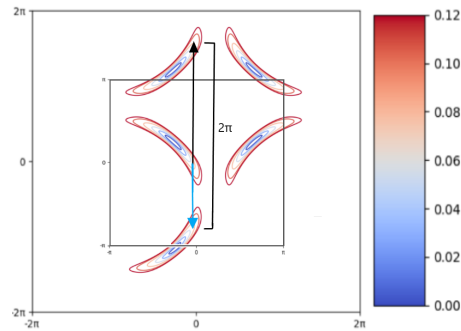


**Figure 2.6:** The black arrow represents the original vector. The vector modulo  $2\pi$  is drawn in blue. Only because of the additional contour there exists such a vector. Of course in order for all vectors to be periodic the underlying CCE's also have to be fully periodic.

taking a perfectly periodic Fermi surface seems legitimate. A visualisation of why different vectors modulo  $2\pi$  are equivalent for a periodic Fermi surface is shown in Fig. 2.6.



# Modelling the scattering

## 3.1 Tight-binding model

In order to obtain the LDOS it is necessary to parametrize the dispersion relation of the material in question. A general way of doing this is using the tight-binding model. In this model the electrons are assumed to be closely bound to their respective nuclei, and have only a chance to move to another atom. The generic dispersion relation for the tight-binding model looks like

$$\begin{aligned} \epsilon(\mathbf{k}) = & -2t_0 * [\cos(k_x) + \cos(k_y)] - 4t_1 * \cos(k_x)\cos(k_y) \\ & - 2t_2 * [\cos(2k_x) + \cos(2k_y)] - 4t_3 * [\cos(2k_x)\cos(k_y) + \cos(k_x)\cos(2k_y)] - \mu \end{aligned} \quad (3.1)$$

Here  $t_i$  is a hopping parameter, which can be roughly interpreted as the possibility that an electron moves from one nucleus to another. The  $\mu$  term is the chemical potential which can be seen as the amount of charge in the system at every location. Later the chemical potential will be used to implement the doping of the system. It is assumed also that  $\mu$  is the only way the system depends on the doping. So once the  $t_i$ 's are determined for the system, they are representative as long as the tight-binding approach does not break down. For a good fit of the cuprates, at least hopping to the next-nearest neighbour is required. This corresponds to using parameters up to  $t_1$ . However, in order to get the most detailed dispersion relation we use the parameters given by the supplementary material of Hoffman *et al.* [14] for Bi-2201. These parameters are given by:  $t_0 = 0.22$ ;  $t_1 = -0.034315$ ;  $t_2 = 0.035977$ ;  $t_3 = -0.0071637$ . Both the hopping parameters and the chemical potential have dimension of energy and are expressed

in electronvolt (eV). Having obtained the dispersion relation for ordinary electrons in solids we again turn our mind to the dispersion relation of the Bogoliubov quasiparticles. Reprinting Eq. 2.5 for convenience, it is a matter of filling in the dispersion relation for normal particles Eq. 3.1 and the gap function Eq. 2.1.

$$E(\mathbf{k}) = \sqrt{\epsilon_{\mathbf{k}}^2 + \Delta_{\mathbf{k}}^2} \quad (2.5')$$

The new-found dispersion relation can easily be plotted and is shown in Fig. 3.1b next to the dispersion relation for the non-superconducting state. In the case of Bogoliubov quasiparticles the dispersion relation flips up at the Fermi energy because of the square root in Eq. 2.5. This flipping is peculiar to superconductors, and caused the zero LDOS in the gap. The spectrum now has two branches of dispersion. The old winglike part at the corners, and the central bulge. The difference between these branches resides in the fact that Bogoliubov quasiparticles are a linear combination of electrons and holes. The wing parts are the electron-like branch, the bulge is the hole-like branch. In the electron-like branch the coefficients of the electrons increase with higher energy and the hole coefficients decrease. Therefore at high enough energy this branch returns to just behaving as electrons. The same goes for the bulge-branch but then it reduces to a hole band. As a rule of thumb, only around an energy of  $\approx \pm 2\Delta$  [13] the Bogoliubov quasiparticles are truly quasiparticles. The d-wave gap however allows the Fermi surface not to be completely gapped in the official gap range. For the gap size parameter we choose  $\Delta_0 = 0.01$  Ev[15], to be implemented in Eq. 2.1.

Having set all parameters we are now free to choose  $\mu$  to appropriately simulate the experimental results. For the samples attempted to be reproduced only the critical temperature was known. Setting  $\mu$  can be done in two ways for such samples. Firstly, for a given  $\mu$  the doping can be calculated. This can be done by first counting all states under the Fermi energy. To obtain the average occupation,  $\langle n \rangle$ , then the fraction of occupied states versus total states is calculated. The total states being the amount of allowed momentum states multiplied by two because of spin degeneracy. The doping follows from  $p = 1 - \langle n \rangle$ . Then from the phase diagram the corresponding critical temperature can be gauged. If the critical temperature of the material differs from the one given for  $\mu$  the chemical potential can be tweaked accordingly. Doping however can be a bit ambiguous, especially in the overdoped phase. Therefore the preferred method is just fitting the calculated QPI to the experimental data by trial and error. By now for several critical temperatures the value for  $\mu$  is known. Extrapolate

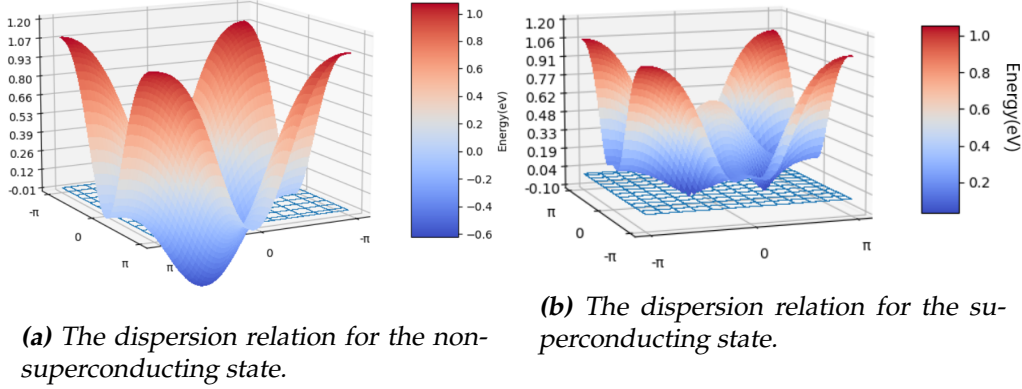


**Figure 3.1:** The dispersion relations for Bi-2201 due to a tight-binding fit. The surface flips up around the gap as it is supposed to. Due to the nature of the  $d$ -wave gap the Fermi surface still exists in the gap. The gap has been exaggerated to  $\Delta = 0.2$  for clarity.

lating from these values to other  $T_c$ 's is much easier. We need two known points from Hoffman *et al.* [14]. For optimally doped their paper obtained  $\mu = -0.21$  with  $T_c = 35\text{K}$ . For overdoped the value was  $\mu = -0.25$  with  $T_c = 15\text{K}$ . Both were obtained using the joint density of states (JDOS) method, to be explained in the next section. Hence we choose  $\mu = -0.255$  for the simulation at 12K. Furthermore we will choose  $\mu = 0.235$  to simulate OD23K and  $\mu = 0.28$  to simulate OD3K.

## 3.2 Autocorrelation

The simplest method to qualitatively reproduce the QPI pattern is by using an autocorrelation function. As could be glanced from Eq. 2.10, the scattering can be somewhat approximated by setting all coherence factors and  $|V|$  to unity. The scattering then reduces to the product of two densities of state. Calculating this quantity for all  $k_i$  basically amounts to taking the autocorrelation of the Fermi surface. The formula for this joint density of states (JDOS) is given by:

$$JDOS(\mathbf{q}, E) = \int_{BZ} A(\mathbf{k}, E) A(\mathbf{k} + \mathbf{q}, E) d\mathbf{k} \quad (3.2)$$

Here  $A(\mathbf{k}, E)$  is called the spectral function. In this case  $A(\mathbf{k}) = \epsilon(\mathbf{k})$ , for the energy range of which the JDOS is to be calculated. Out of these bounds  $A(\mathbf{k}) = 0$ . For the JDOS-calculation to work it is necessary for

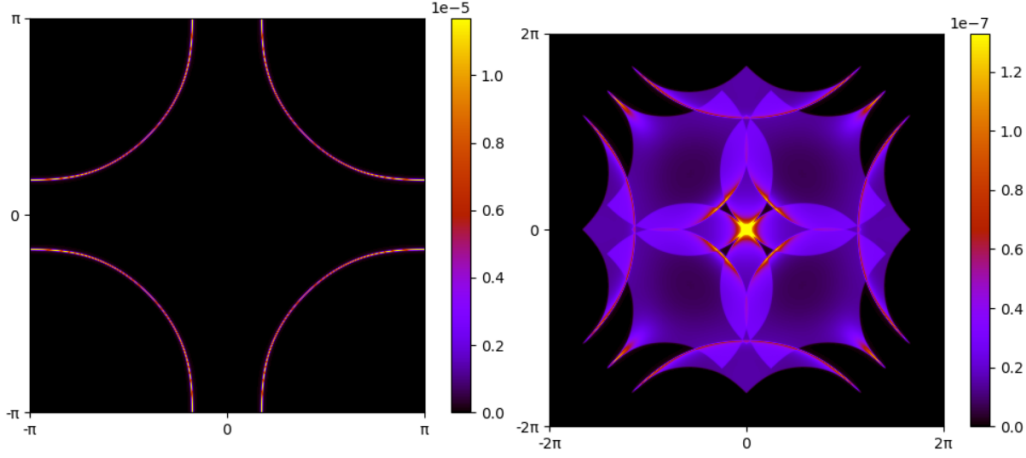
both the lattice of the Fermi surface to be sufficiently large and for the energy range to be sufficiently broad. Generally a grid size of 1000x1000 pixels is taken. The thermal broadening taken is of a temperature of 4K, the temperature of the samples. This gives a thermal broadening of roughly  $4k_bT \approx 1.44$  meV. An example of the QPI resulting from a Fermi surface can be seen in Fig. 3.2. An interesting observation regards the way autocorrelations are easily calculated. The quick way to calculate the autocorrelation is by squaring the inverse Fourier transform of the spectral function, and then Fourier transforming it back. Because both this autocorrelation and the T-matrix rely on this calculation a quick proof is given. The basic idea is to write the spectral function as a Fourier decomposition in its real space components. So substituting  $A(\mathbf{k}) = \frac{1}{\sqrt{2\pi}} \int d\mathbf{r} A(\mathbf{r}) e^{-i\mathbf{k}\cdot\mathbf{r}}$  in Eq. 3.2 we get

$$\begin{aligned}
 JDOS(\mathbf{q}, E) &= \frac{1}{2\pi} \int_{BZ} \int d\mathbf{r} A(\mathbf{r}, E) e^{-i\mathbf{k}\cdot\mathbf{r}} \int d\mathbf{l} A(\mathbf{l}, E) e^{-i(\mathbf{k}+\mathbf{q})\cdot\mathbf{l}} d\mathbf{k} \\
 &= \frac{1}{2\pi} \int d\mathbf{r} \int d\mathbf{l} \int_{BZ} e^{-i(\mathbf{r}+\mathbf{l})\cdot\mathbf{k}} d\mathbf{k} A(\mathbf{r}, E) A(\mathbf{l}, E) e^{-i\mathbf{q}\cdot\mathbf{l}} \\
 &= \frac{1}{\sqrt{2\pi}} \int d\mathbf{r} \int d\mathbf{l} \delta(\mathbf{r} - \mathbf{l}) A(\mathbf{r}, E) A(\mathbf{l}, E) e^{-i\mathbf{q}\cdot\mathbf{l}} \\
 &= \frac{1}{\sqrt{2\pi}} \int d\mathbf{r} [A(\mathbf{r}, E)]^2 e^{-i\mathbf{q}\cdot\mathbf{r}}
 \end{aligned} \tag{3.3}$$

The result is clearly the Fourier transform of the square of the real-space spectral function.

### 3.3 T-matrix method

The first application of the T-matrix to cuprates was by Wang *et al.* [4]. Their method resulted in qualitative agreement, but the peaks they observed were not of the right intensity and sharpness. Though over the years the results improved somewhat, the main conclusion was that the T-matrix method could only qualitatively reproduce the octet model, but not quantitatively [4] [16] [17]. In order to explain the theory behind the T-matrix method some quantum field theory machinery is necessary. To remain as lucid as possible a hybrid approach combining Balatsky *et al.* [9], Hussey [18] and Joynt [19] will be used. So as to keep things tractable we will simply start out with a reduced mean-field BCS Hamiltonian,



(a) The Fermi surface at  $E=0$  for an underdoped cuprate. The gap is set to zero for clarity. (b) The JDOS calculation for the Fermi surface given in the left image.

**Figure 3.2:** The result of the autocorrelation calculation. Notice how the size of the space doubles.

of which the derivation can for example be found in for example Tinkham [13]. Immediately writing the mean-field BCS Hamiltonian in a Nambu basis results in

$$H_0 = \sum_k \Psi_k^\dagger (\epsilon_k \sigma_3 + \Delta_k \sigma_1) \Psi_k \quad (3.4)$$

$$H_{imp} = \sum_{kk'} \Psi_k^\dagger U_{kk'} \sigma_3 \Psi_{k'}. \quad (3.5)$$

The completely Hamiltonian is the sum of these terms. Because the equation is written in a Nambu basis we have  $\Psi_k^\dagger = (a_{k\uparrow}^\dagger, a_{-k\downarrow})$ . The  $a_k^{(\pm)}$ 's are again the annihilation (creation) operators for electrons. The spinor  $\Psi_k^\dagger$  is equivalent to the Bogoliubov operators from Eq. 2.3, as it creates a quasiparticle. As usual the  $\sigma_i$  are the Pauli spin matrices. The Green's function is now defined as the time ordered average of these spinors, given by

$$G_{kk'} = -\langle T \Psi_k \Psi_{k'}^\dagger \rangle. \quad (3.6)$$

Getting the evolution in time for these operators can be done through using the Heisenberg picture:  $\frac{\partial}{\partial \tau} \Psi = [H_{BCS}, \Psi]$ . In order to proceed Wick's theorem or Feynman diagrams can be used. Both cases result in calculating the Feynman propagator. Solving for the unperturbed Hamiltonian

$$G_{0k} = \frac{1}{(\omega + i\eta)\sigma_0 - \epsilon_k \sigma_3 - \Delta_k \sigma_1}. \quad (3.7)$$

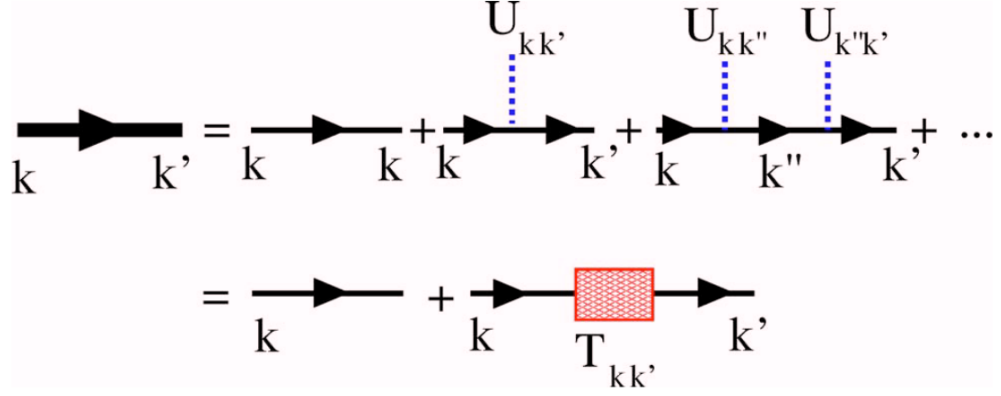


**Figure 3.3:** A schematic showing how to express  $G_{kk'}$  in  $G_{0k}$  and  $U_{kk'}$ . The thick black line on the left hand side corresponds to the perturbed Green's function  $G_{kk'}$ . The thinner lines indicates the unperturbed Green's function  $G_{0k}$ . As can be seen the total scattering is the sum several iterative scatterings using the unperturbed Green's function. All these scatterings can be encapsulated in the T-matrix.

The  $i\eta$  is added to ensure the analytic continuation of the Green's function. Of course what remains is to calculate the perturbed Green's function  $G_{kk'}$ . Luckily we can express  $G_{kk'}$  in terms of  $G_{0k}$ . Observing that the full scattering consists of a sum of scattering processes for the unperturbed Green's function, as shown in Fig. 3.3, we can write

$$G_{kk'} = G_{0k} + G_{0k}U_{kk'}G_{0k'} + \sum_{k''} G_{0k}U_{kk''}G_{0k''}U_{k''k'}G_{0k'} + \dots \quad (3.8)$$

$$= G_{0k} + G_{0k}T_{kk'}G_{0k'}. \quad (3.9)$$

With the T-matrix given by

$$T_{kk'} = U_{kk'} + \sum_{k''} U_{kk''}G_{0k''}U_{k''k'} + \dots \quad (3.10)$$

$$= U_{kk'} + \sum_{k''} U_{kk''}G_{0k''}T_{k''k'}. \quad (3.11)$$

The scattering potential  $U$  is written as a combination of magnetic and potential scattering given by

$$U_{kk'} = V_{kk'} \otimes \sigma_3 + J_{kk'} \otimes I_2. \quad (3.12)$$

Here  $V_{kk'}$  is the scattering potential for a normal impurity and  $J_{kk'}$  is the scattering potential for a magnetic impurity. The equation can be greatly

simplified by assuming the scattering to be isotropic, and hence take  $U_{kk'}$  to be independent of  $k$ . If this assumption is made, T can be written as

$$T(\pm\omega) = \frac{\pm(V \otimes \sigma_3 + J \otimes I_2)}{1 - (V \otimes \sigma_3 + J \otimes I_2)g_0(i\omega)} \quad (3.13)$$

with

$$g_0 = - \sum_k \frac{1}{\pi N} G_{0k} \quad (3.14)$$

to solve the self-consistent equation. Substituting Eq. 3.13 in Eq. 3.11 proves the point. In order to calculate the total scattering the perturbed Green's function should be calculated for all  $k$ . This amounts to calculating the integral  $\int dk$ , which reduces the problem to almost exactly the JDOS calculation in Eq. 3.3. Thus the scattering is easier to calculate in real space, therefore we write

$$G_{rr'} = G_{0r} + G_{0r} T G_{0r'}. \quad (3.15)$$

In order to calculate the QPI pattern in q-space, now Eq. 3.15 only has to be Fourier transformed. Having obtained the Green's function and the T-matrix some physical interpretation is in place. Simply put we have

$$LDOS(\omega, \mathbf{k}) \propto -\frac{1}{\pi} \text{Im} \left( \int d\mathbf{r} G_{rr'}(\omega, \mathbf{r}) e^{i\mathbf{k} \cdot \mathbf{r}} \right) \quad (3.16)$$

Since  $G_{rr'}$  is a 2x2 matrix we have two densities of state. The imaginary part of the  $G_{rr'}^{11}$  element is interpreted as the density of electron states. With the same constraints the  $G_{rr'}^{22}$  element represents the hole density of states. Naively for STM measurements it is assumed only the  $G_{rr'}^{11}$  is needed, because the STM solely measures electrons. Later we will try and answer whether that is indeed the case.

### 3.3.1 The effect of the potential

In order to see how the potential affects the Green's function  $G_{rr'}$  we explicitly calculate its elements. Combining Eq. 3.9 and Eq. 3.13 and writing out the elements we get

$$G_{rr'}^{11} = g_0^{11} + G_{0r}^{11} \frac{U^{11}}{1 - U^{11}g_0^{11}(i\omega)} G_{0r'}^{11} + G_{0r}^{12} \frac{U^{22}}{1 - U^{22}g_0^{22}(i\omega)} G_{0r'}^{21} \quad (3.17)$$

$$G_{rr'}^{22} = g_0^{22} + G_{0r}^{22} \frac{U^{22}}{1 - U^{22}g_0^{22}(i\omega)} G_{0r'}^{22} + G_{0r}^{21} \frac{U^{11}}{1 - U^{11}g_0^{11}(i\omega)} G_{0r'}^{12} \quad (3.18)$$

with

$$U^{11} = V + J \quad (3.19)$$

$$U^{22} = -V + J \quad (3.20)$$

As expected the perturbed function  $G_{rr}^{11}$ , mainly depends on the scattering from the unperturbed function  $G_{0r}^{11}$  to  $G_{0r'}^{11}$ . This amounts to electron-electron scattering. The same reasoning holds for the hole part. However of interest is the fact how the scattering intensity depends on the choice of potential. For it is clear that by setting  $V = -J$  all scattering between electrons can be removed, because it reduces  $U^{11}$  to zero. Identically putting  $V = J$  kills the hole scattering. Starting from a scenario where the scattering of either component is extinguished, the potential can slowly be tweaked to balance the different scatterings to the right intensity. Concluding the parallels between the JDOS calculation and the Green's function are touched upon. Comparing with Eq. 3.15 the autocorrelation now makes sense. The JDOS calculation is basically a T-matrix approach with the identity for the T-matrix. Even more succinctly put, in the limit of infinite scattering strength the T-matrix approach and the JDOS become identical up to a proportionality constant and a sign. In this case

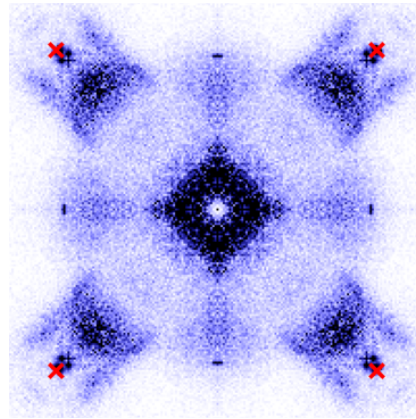
$$T(\pm\omega) = \lim_{U \rightarrow \infty} \frac{\pm U}{1 - U g_0(i\omega)} = \mp \frac{1}{g_0(i\omega)} \begin{pmatrix} 1 & 0 \\ 0 & -1 \end{pmatrix}. \quad (3.21)$$

### 3.4 Addressing non-periodicity in q-space

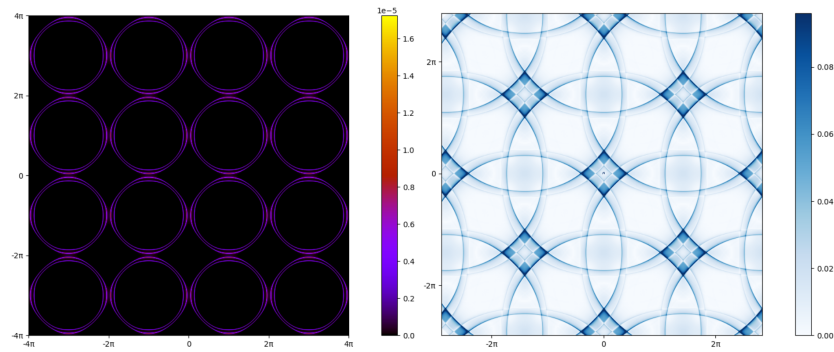
Having obtained a parametrization for the energy, and a way to calculate scattering, we seem ready to simulate experiment. There is however a final discrepancy to address. With the current model, the QPI pattern in q-space would be periodic in  $2\pi$ . When observing the experimental data the periodicity is not seen. As can be glanced from Fig. 3.4a signal intensity drops precipitously beyond the Bragg peaks, causing the q-space to be non-periodic. Physically there can be a speculative explanation for the non-periodic q-space. When simulating a periodic QPI pattern in q-space we assume interference vectors up to an infinite q-length. This in turn implies quasiparticles that start to behave more and more like particles and therefore have more difficulty navigating the disordered lattice. The exact mechanism is however not understood.

While the QPI anisotropy is due to a decrease in scattering between the first Brillouin zone and higher Brillouin zones, we will model the reduction in a different way. To simulate the decrease in scattering the Fermi

surfaces in higher Brillouin zones will be reduced in intensity. The higher the Brillouin zone, the more the Fermi surface will be weakened. Every higher Brillouin zone will be multiplied by  $c^n$  with  $c$  a constant and  $n$  the order of the Brillouin zone. As a result, the calculated QPI pattern will be weakened as if there was less scattering between the Fermi surfaces. Of course now that the strict periodicity of k-space is broken, merely plotting q-space from  $-\pi$  to  $\pi$  does not suffice. To properly compare experiment and theory we will additionally show q-space from  $-2\pi$  to  $2\pi$ . Even more poignant, also within the q-space  $-\pi$  to  $\pi$  the QPI pattern changes if scattering between Brillouin zones is truly weaker. For example, if in Fig. 2.6 the downmost CCE is reduced in intensity, the interference vector lying within  $-\pi$  and  $\pi$  becomes less pronounced. Therefore the litmus test for the model with the weakened Fermi surface is to yield better results in q-space both between  $-\pi$  and  $\pi$ , as well as between  $-2\pi$  and  $2\pi$ . To get a preliminary grasp of how the periodicity of the QPI simulation is broken we show the results for the different approaches. In Fig. 3.4 we show the periodic Fermi surface (Fig. 3.4b) and the resulting QPI pattern (Fig. 3.4c). The pattern is indeed periodic in q-space. Below these in Fig. 3.4e the periodicity of the Fermi surface is broken by weakening higher Brillouin zones with a factor 0.1. The resulting QPI pattern now also decays in q-space. we reiterate that in reality it is decreased scattering that causes the non-periodicity, not the weakening of the Fermi surface.

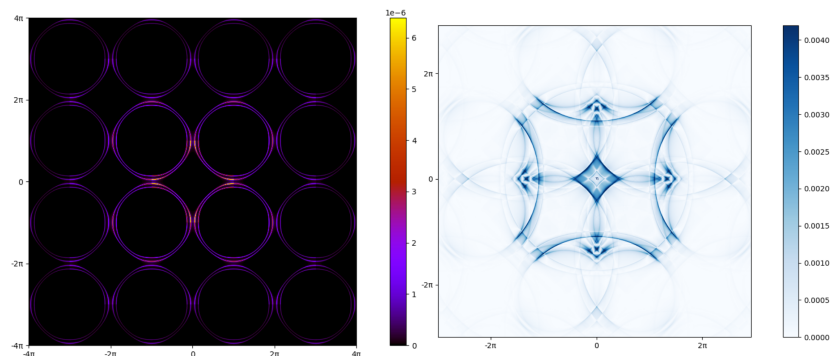


(a) The experimental QPI pattern in  $q$ -space. The Bragg peaks are indicated by the red crosses in the corners of the signal.



(b) The periodic Fermi surface generally assumed for T-matrix simulations.

(c) The simulated QPI pattern resulting from perfect scattering.



(d) The non-periodic Fermi surface used to simulate decreased scattering.

(e) The simulated QPI pattern for a non-periodic Fermi surface.

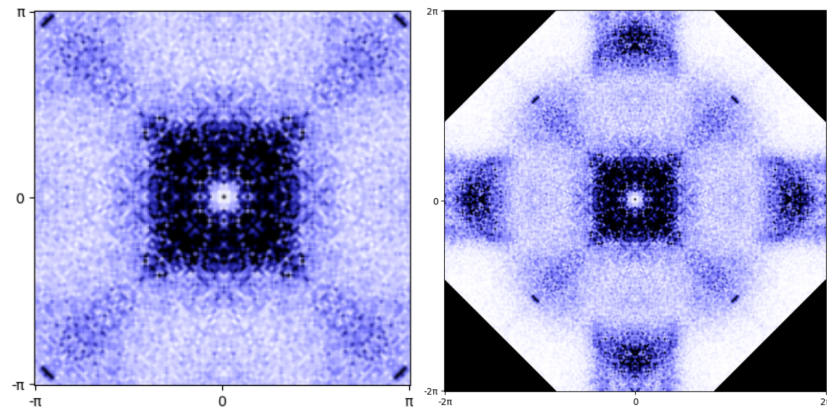
**Figure 3.4:** The breaking of periodicity in  $q$ -space due to the weakening of higher order Brillouin zones in  $k$ -space.

## Results

In this section we will give the results for three subjects. First we will test whether weakening higher Brillouin zones results in better simulations of the experiment. Secondly, we will use the weakening constant resulting from this to investigate whether both electron and hole scattering should be considered in the simulation. During this analysis we will compare both QPI patterns generated with and without gap. Finally we turn to identifying the van Hove singularity in the experimental data with the use of the simulation. In order to obtain quantitative results about the correspondence of images we have used the Structural Similarity Index Measure. This index developed by Wang *et al.*[20] provides a way of comparing images more reliably than root-mean-square calculations of the intensities. A slight elaboration on the algorithm can be found in the appendix, including the steps taken to fit the data to the algorithm. A higher SSIM value means a better fit. In order to be consistent with theoretical literature we will rotate the experimental image to align it along the  $q_x$  and  $q_y$  axis. The comparison will be performed for three different dopings.

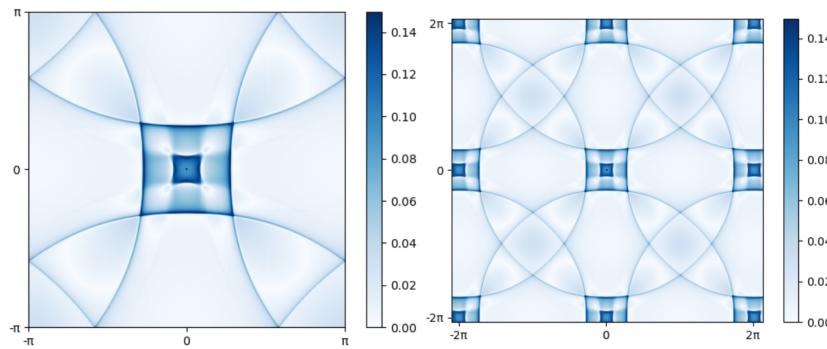
### 4.1 Breaking of periodicity in q-space

To truly be able to conclude that breaking the periodicity of q-space provides better results we will compare experiment and simulation at three different q-space sizes. The lengths range from  $-\pi$  to  $\pi$ ,  $-2\pi$  to  $2\pi$  and finally the full experimental image. Although not completely appropriate, for convenience we will refer to  $-\pi$  to  $\pi$  as the first Brillouin zone in q-space, and to  $-2\pi$  to  $2\pi$  as the second Brillouin zone.



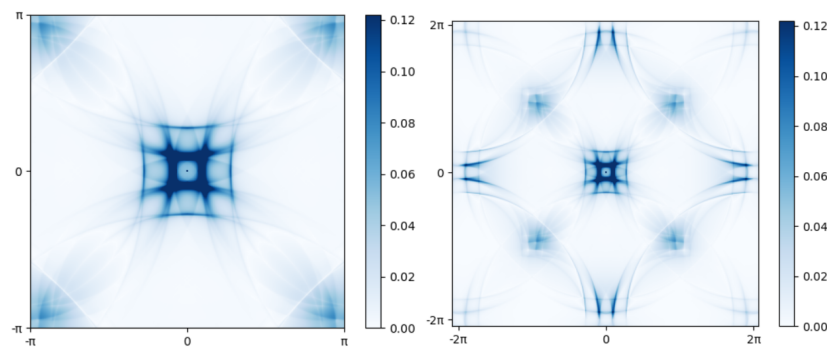
(a) The experimental QPI pattern of the first Brillouin zone in  $q$ -space.

(b) The experimental QPI pattern of the second Brillouin zone in  $q$ -space.



(c) The theoretical QPI for a perfectly periodic Fermi surface in the first Brillouin zone.

(d) The theoretical QPI for a perfectly periodic Fermi surface in the second Brillouin zone.



(e) The theoretical QPI for a Fermi surface that is weakened by 0.1 for every higher zone. The first Brillouin zone is shown.

(f) The theoretical QPI for a Fermi surface that is weakened by 0.1 for every higher zone. The second Brillouin zone is shown.

**Figure 4.1:** The different results for the first and second Brillouin zone.

The first two zones both for experiment and simulation are shown in Fig. 4.1. When applying the SSIM the generated QPI is rotated instead of the experimental as is shown here. Furthermore the strength with which the Fermi surface is reduced is also varied. The constants chosen are 1, 0.5, 0.1 and 0. As already mentioned, the higher order Brillouin zones will be multiplied by these constants. Thus  $c=1$  means that the Fermi surface is still perfectly periodic. For the strength of the scattering potential we take  $V=-0.05$  eV and  $V_m = 0.04$  eV for the calculations with only electrons. Crucially the scattering potential for both electrons and holes, to be used later, will be set to  $V=-0.05$  and  $V_m=-0.026$ . The gap is set to 10 meV according to Li *et al.*[15]. Since the gap is more likely to fill than close this gap is chosen for all dopings. The SSIM values comparing simulated patterns with experiment for all these parameters are shown in Fig. 4.5.

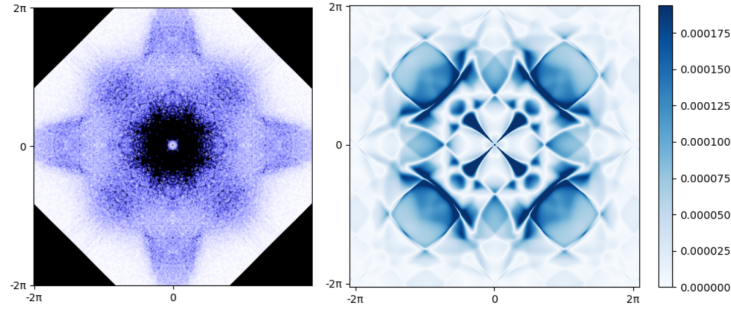
## 4.2 Filling the gap

Our preliminary results show that a QPI pattern generated with  $C=0$  yields the best fit. Because setting the higher order Fermi surfaces to zero is somewhat unphysical we will choose a weakening constant of 0.1 for further simulations. Though the modelling works reasonably well, there is still an important aspect of the simulated QPI that we have neglected so far. While the fits at higher energies are quite representative, the simulation at energy close to and especially at  $E=0$  is not. The experimental data for  $E=0$  is given in Fig. 4.2a. The simulation with a gap is given in Fig. 4.2b. Clearly large parts of the required pattern are missing. As mentioned earlier this might be to the filling of the gap. An image showing the QPI pattern with the gap set to zero is shown in Fig. 4.2c. Because the no-gap image seems more representative we will compare QPI patterns with zero gap to patterns with normal gap. The result of this comparison is shown in Fig. 4.6.

## 4.3 Adding holes

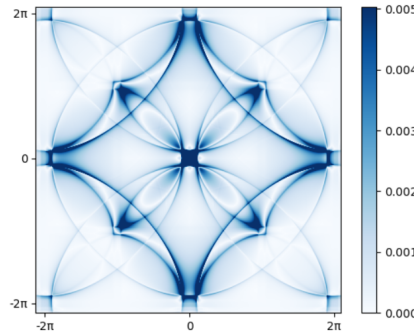
The images achieved by extending k-space and filling the gap are a huge improvement. However, the correspondence is still not perfect. From the patterns generated we can glance three possible areas of improvement, indicated by the colored circles in Fig. 4.3.

Firstly, the center of the experimental images (Fig. 4.3a) has a much higher intensity than the pure electron simulation (Fig. 4.3b). Also, their



(a) The experimental data for OD3K at 0 meV.

(b) The simulated QPI pattern of OD3K at 0 meV. The gap is still 10 meV.



(c) The simulated QPI pattern of 3K at 0 meV. The gap is set to zero.

**Figure 4.2:** To observe the filling of the gap experimental data is compared with simulated data without gap and with simulations of where the gap and no-gap pattern have been combined.

form does not corresponds exactly to experiment. Secondly, in between the corners of the arcs of the experimental data the intensity is higher than in the simulation. This location is indicated by the red circle. Finally the lack of a central square, indicated by the orange circle, could be improved. In order to increase the intensity an approach suggested by Wang [4] and Hirschfelt *et al.* [21] is taken. The authors propose that for broken SU(2) symmetry in spin space, the hole density of states also has to be taken into account when calculating the QPI pattern. The new density of states therefore reads:

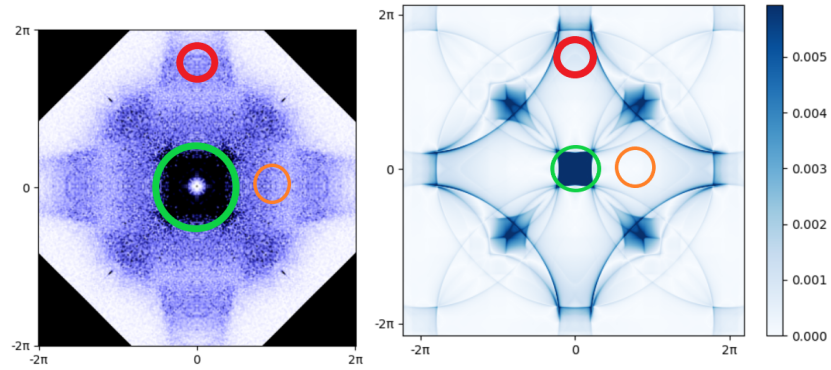
$$LDOS(\mathbf{k}, E) = -\frac{1}{\pi} \text{Im}(G_{kk}^{11}(\mathbf{k}, \omega) - G_{kk}^{22}(\mathbf{k}, -\omega)) \quad (4.1)$$

The reason this might work is that at positive energies the hole bands are

closer together than the electron bands. Therefore the scattering vectors will be shorter, which will result in an increase in the density of states around the center. In order to observe the maximal effect we choose a high energy. At higher energies the electron and hole band are farther apart and therefore their impact should be better recognizable. The results of comparing electrons only versus electrons and holes are shown in Fig. 4.6.

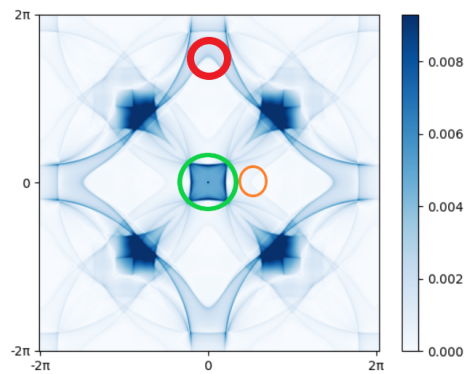
## 4.4 The van Hove singularity

Finally being able to agreeably simulate the QPI pattern we turn to analysing the experimental images. For example, an interesting question is whether the van Hove singularity is seen in the data. From Fig. 3.1b we can see that the vHS lies at  $\vec{q} = (\pm\pi, 0)$  and  $\vec{q} = (0, \pm\pi)$ . Therefore the value of the vHS for the model can be calculated by substituting these values in Eq. 2.5. This yields  $vHS_{23K} \approx 0.047eV$ ,  $vHS_{12K} \approx 0.028eV$  and  $vHS_{3K} \approx 0.010eV$ . Although the intensity of the peaks in the QPI measurement Fig. 4.4b does speculatively suggest its presence, proving it would be worthwhile. To show what part of the measurement can be contributed to the vHS the Fermi surface was masked before the QPI calculation. All parts of the Fermi surface not showing the vHS were blocked out. That way all QPI signal can be attributed to the diverging DOS. The masked Fermi surface is shown in Fig. 4.4a. The general padding of the surface was applied, but for clarity this is not shown. The result of the QPI calculation with reduced Fermi surface is shown in Fig. 4.4c. A final interesting observation was that the vHS is also visible at plus 30 meV. The comparison of the vHS above the Fermi energy with experiment can be found in the appendix.



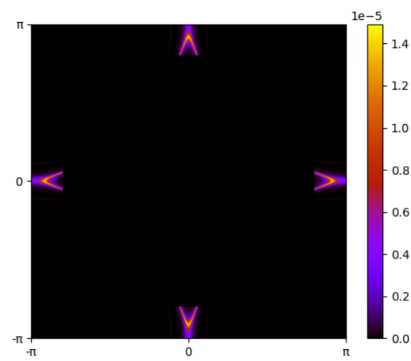
(a) The experimental data for OD3K.

(b) The simulated QPI pattern for only the electron band with a gap of 10 meV.

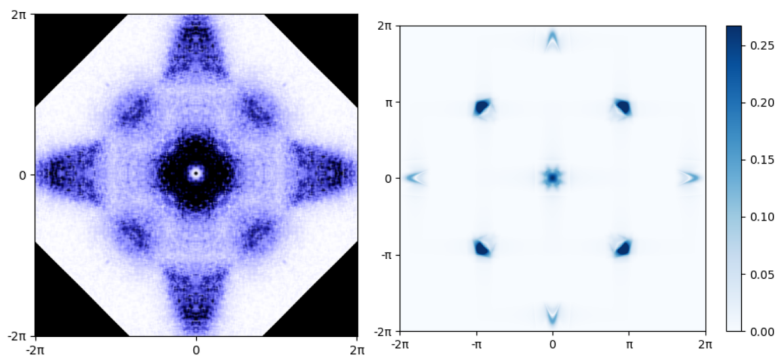


(c) The simulated QPI pattern with both the electron and hole band with a gap of 10 meV.

**Figure 4.3:** The differences between only modelling the electron band and modelling both the electron and hole band. All simulations are made at OD3K at 50 meV. Areas of interest are circled.



(a) The partially masked Fermi surface at the vHS.



(b) The experimental data for OD12K at -30 meV.

(c) The simulated QPI pattern resulting from the masked Fermi surface.

**Figure 4.4:** Comparison between experiment and the QPI of the masked Fermi surface at -30 meV.

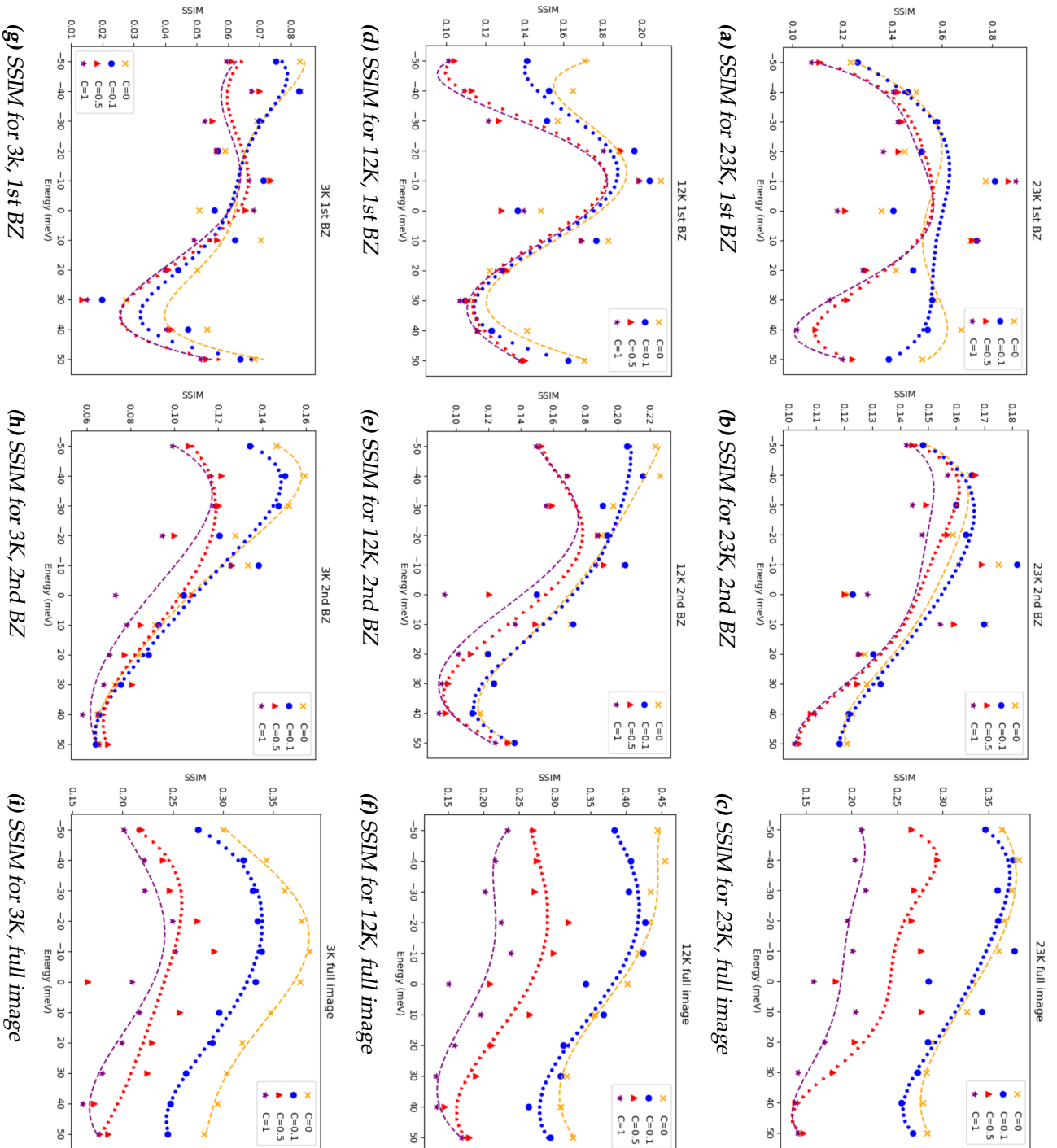
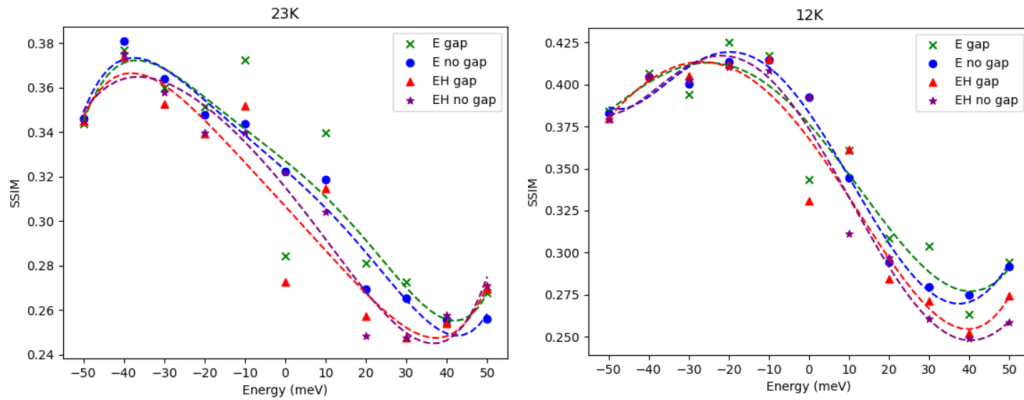
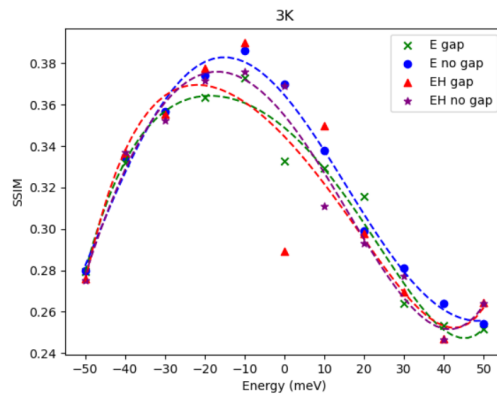


Figure 4.5: The SSIM values for different weakenings of the QPI. The higher  $C$ , the more periodic the QPI pattern.



(a) The SSIM values for different energies in OD23K.

(b) The SSIM values for different energies in OD12K.



(c) The SSIM values for different energies in OD3K.

**Figure 4.6:** The results of simulating only electrons and both electrons and holes. Also the results for setting the gap to zero are given.



## Discussion

Having both the SSIM for quantitative analysis and the images for a qualitative analysis we are in a position to discuss the results. Before starting of, a caveat is in place. To compare images quite some manipulations have to be performed to substitute the data in the algorithm. Henceforth the results may not always be reliable. Especially the fact that the experimental images are fed into the algorithm, instead of the raw data makes vigilance about the results necessary. Additionally as can be seen in the appendix a cut-off is necessary when turning simulation images into greyscale. This only influences central peak intensity.

### 5.1 The periodicity of q-space

In Fig. 4.5 the SSIM values for different weakenings of the higher Brillouin zones are given. Firstly, we observe that on average a stronger breaking of the periodicity gives better results. Especially at the extremes of the energy scale the simulation with broken periodicity prevails. Logically the difference in SSIM is biggest when comparing the simulation with the full experimental image. This conclusion is also supported by qualitatively comparing images, where we indeed see that the QPI signal after the second Brillouin zone rapidly drops off. The telling sign that there really is reduced scattering between higher BZ's is given by looking at the first Brillouin zone SSIM values (Fig. 4.5a, Fig. 4.5d and Fig. 4.5g). The difference between different weakenings is smallest here. Such is expected, considering that most of the signal in this area results from scattering within the first Brillouin zone in k-space. However, there is signal in the first Brillouin zone that actually does depend on the periodicity of the lattice. The

fluctuating signal is the result of the peaks that would otherwise extend beyond the first zone. Though not beyond doubt, it is probably the decrease in intensity of these areas that causes a better fit with experiment. When looking at Fig. 4.1c and Fig. 4.1e it is likely that the difference in arc intensity causes the change in SSIM values. Interestingly the main region where the SSIM deviates from showing  $C=0$  on top is between  $-10$  meV and  $+10$  meV. This does for example happen in Fig. 4.5a. Though hard to say for certain, the deviation might result from the fact that the gap is set at  $10$  meV. Therefore the DOS peak lies around this energy. Either the simulation is not capable of representing this peak correctly, or because of the high DOS the simulated images are harder to substitute into the algorithm. We always need renormalise the data to the interval  $-1$  to  $1$ . When there are extreme values in the original, these have to be carefully removed to prevent them from spoiling the signal. Otherwise the extreme values are set to one, and all else to  $-1$ . That way the algorithm can't compare properly. At  $E=0$  also something interesting happens. Both in Fig. 4.5a and Fig. 4.5d we see that the SSIM deteriorates. The deterioration might be due to filling of the gap. The filling is not modelled and therefore the simulation might resemble the experiment less. However, we would expect the fit to be worst in the most overdoped scenario. But looking at the most overdoped cuprate, Fig. 4.5g the SSIM value is not significantly lower. Fascinatingly, the order of breaking constants is reversed here. Perhaps the additional signal generated by the periodicity in  $q$ -space gets mistaken for the filling of the gap.

## 5.2 Including holes in the model

Observing the quantitative results in Fig. 4.6 the possibility of improving the simulation by including holes is dissolved. Practically at every point the electron simulation surpasses the combined simulation. The difference is not massive, but nevertheless stubbornly present. A very important remark here is that in order to obtain almost equal SSIM values for both simulations the potentials had to be different. As mentioned here the potentials used were  $V=-0.05$  eV and  $V_m = 0.04$  eV for the calculations with only electrons and for both electrons and holes  $V=-0.05$  and  $V_m=-0.026$ . If the electron simulation uses the scattering for the combination simulation the SSIM value drastically change. In such a case it actually seems that using both holes and electrons is an improvement. The reason why we need the specific electron parameters is that we need to maximize the scattering between the non-diagonal elements of the Green's function. These  $G_{12}$

and  $G_{21}$ -terms are dependent on the gap and scatter through the imaginary part of  $T_{22}$ . As  $T_{22}$  is determined through  $T_{22} = V - V_m$  it will be more sizable than  $T_{11}$  when  $V$  and  $V_m$  have opposite sign and are about equal. In retrospect the whole venture of adding holes to solve a problem with intensities for the T-matrix approach seems rather hubristic. The model is known to deviate from experiment in especially the intensities. Adding holes to solve the deficiency only makes things worse.

### 5.3 Setting the gap to zero

Looking at the quantitative results in Fig. 4.6 there is tentative evidence that setting the gap to zero in the simulation could be an improvement occasionally. Though soundly beaten everywhere above the gap, the zero-gap simulation performs better than the gap simulation at  $E=0$ . On the basis of our qualitative analysis of Fig. 4.2 this makes sense. The difference is so immense that even the "bad" simulation of both electrons and holes with gap set to zero is better than the "good" simulation of pure electrons with a non-zero hole. In future simulations a method to simulate the filling of the gap should definitely be included. Of course this also corresponds to experiment where the filling of the gap is tentatively seen.

### 5.4 Final remarks

Two additional observations can be made. Interestingly, the overall highest SSIM score is obtained for the 12K case. Fascinatingly enough this was also the doping for which the closest value of  $\mu$  was known. Though the chemical potential was determined by a combination of doping calculations, literature and qualitative analysis it might very well be that the SSIM could be improved by better choosing  $\mu$ . The reverse is of course also true. By trying different values of  $\mu$  and calculating the SSIM, the best fit and hence the doping could theoretically be determined. The other observation is that the SSIM values tend to decrease at higher energies for the full image and the second BZ. Only a guess can be ventured, but a plausible explanation would be that the scattering potentials are not properly chosen. At the higher energy ranges the hole van Hove might very well play an important role, and up or down tuning its intensity could prove key to flattening the curve. This tuning can of course be done by more judiciously choosing the scattering parameters.



## Conclusion and outlook

The goal of research was applying the T-matrix method to simulate QPI in overdoped cuprates. The T-matrix was originally intended for use on underdoped cuprates. Its incipency was caused by the observation that in the underdoped regime there were clearly defined peaks in the QPI-signal. Knowing the arc-like nature of the Fermi surface, Wang *et al.* [4] deduced that the QPI-pattern had to arise from scattering between the locations of high DOS at the tips of these arcs. Thus the T-matrix approach was developed. This approach qualitatively corresponded to the experiments. The peaks however were not of the right intensity, and were lacking the correct sharpness.

Extending the T-matrix approach to the overdoped regime was not trivial because the application to underdoped cuprates already gave these mixed results. Making things worse, the octet-model relied on for underdoped materials breaks down in overdoped cuprates. When using the octet model sometimes a peak folded back, but it could nevertheless be easily indentified. In the overdoped case, entire arcs folded back into the Brillouin zone. If the QPI pattern were perfectly periodic this would be no problem. The entire q-space can in such a case be understood from the first Brillouin zone. From experiment it was very clear however, that the QPI signal was far from periodic. At and beyond the Bragg peaks the signal intensity deteriorates quickly. Therefore it was crucial to properly expand the T-matrix into at least the second Brillouin zone. The suggestion to do so was to weaken the Fermi surface in k-space for higher Brillouin zones. Thereby the break down of perfect scattering between all Brillouin zones is simulated, and the periodicity in q-space is broken. To verify that this slightly unphysical approach truly yielded better results the Structural Similarity Index Measured was used. As a quantative measure of

similarity, it can be used to reinforce or undermine qualitative observations. To prove the correctness of the suggested improvement, simulation was compared with experiment for three different dopings and all relevant Brillouin zones. To find the optimal weakening also four different breaking constants were compared. From this analysis resulted the conclusion that weakening the Fermi surface definitely improved the simulation. The vastest improvement was obtained when comparing the full image, but even for the first Brillouin zone breaking the periodicity in  $k$ -space yielded a better simulation. Because of this approach it was finally possible to generate QPI patterns actually resembling the experiments in overdoped cuprates using the T-matrix method.

First the T-matrix was used to check whether both the electron and hole band had to be included for proper QPI results. Applying the SSIM to compare measurements with simulation the answer sounded negative. Secondly through comparing gapped and non-gapped QPI patterns a check was performed testing whether the superconducting gap really fills when increasing doping. The answer to that question sounded affirmative, as the non-gapped simulation outperformed the gapped ones at  $E=0$ . For future application this deficiency of the T-matrix within the gap should be remedied. For better simulating the filling of the gap introducing more scatterers into the T-matrix is recommended. Thirdly the improved method was used to identify the van Hove singularity in the QPI patterns. By masking the non-van Hove part of the Fermi surface it could be shown that the areas of high intensity were definitely due to the aforementioned singularity.

For future research the combination of the T-matrix and SSIM seems quite synergetic. Because of the speed of the T-matrix it is easy to generate simulated data for a lot of different parameters. The SSIM can then be used to prune these solutions to find the optimal values for the variables. As the T-matrix relies on parameters in both the scattering strength and chemical potential there is plenty of room to further improve the simulations. For example, having even better simulations could allow for determining the width of the van Hove singularity in real space. As we have been able to identify which part of the QPI signal causes the signal intensities, an inverse Fourier transform should yield its real space form. Theoretically also the doping of a sample can be determined from studying the QPI measurement and finding the chemical potential with the best fit. There have been other methods that generate a  $q$ -space of the right size. This has been done either by the JDOS calculation [3] or by using Wannier functions [22] after diagonalising a real space Hamiltonian. As the T-matrix is more detailed than the JDOS calculation, and quicker than the Wannier function,

it is a usefull addition to the arsenal for studying QPI. Anyway, through correctly expanding the size of q-space and the the use of SSIM we hope to have added a droplet to the vast ocean of knowledge about simulating quasi-particle interference.

## **Acknowledgements**

First and foremost I am eternally grateful to Willem Tromp and Miguel Sulangi. Their patience with all my ridiculous ideas borders on the divine. Willem I would especially like to credit with surviving an onslaught of theoretical speculations, while Miguel replied always extremely quickly to the most simplistic questions about the code. His answers were sublimely accurate and elaborate. Further my gratitude extends to professor Schalm and professor Zaanen for giving an experimentalist the chance to participate in their group. Sometimes this led to vigorous discussions, but it was always interesting. My special thanks to professor Schalm who despite his incredibly busy schedule would always make time when really necessary. To finish my deepest appreciation for Irene Battisti and again Willem Tromp for obtaining the gorgeous STM images. Without them this whole project would have been impossible.

# Bibliography

- [1] J. G. Bednorz and K. A. Müller, *Possible high $T_c$  superconductivity in the BaLaCuO system*, *Zeitschrift für Physik B Condensed Matter* **64**, 189 (1986).
- [2] J. Friedel, *Metallic alloys*, *Il Nuovo Cimento* (1955-1965) **7**, 287 (1958).
- [3] J. E. Hoffman, *A Search for Alternative Electronic Order in the High Temperature Superconductor Bi $2$ Sr $2$ CaCu $2$ O $8+\delta$  by Scanning Tunneling Microscopy*, PhD Thesis **6**, 57 (2003).
- [4] Q.-H. Wang and D.-H. Lee, *Quasiparticle scattering interference in high-temperature superconductors*, *Phys. Rev. B* **67**, 020511 (2003).
- [5] James Slezak, *Unit cell of Bi-2212, a high-temperature superconductor*, 2014, Online; Accessed: 7-1-2021.
- [6] J. L. Tallon, R. G. Buckley, P. W. Gilberd, M. R. Presland, I. W. M. Brown, M. E. Bowden, L. A. Christian, and R. Goguel, *High- $T_c$  superconducting phases in the series Bi $2.1$ (Ca, Sr) $n+1$ Cu $n$ O $2n+4+\delta$* , *Nature* **333**, 153 (1988).
- [7] B. Keimer, S. A. Kivelson, M. R. Norman, S. Uchida, , and J. Zaanen, *From quantum matter to high-temperature superconductivity in copper oxides.*, *Nature* **518**, 179 (2015).
- [8] C. C. Tsuei, J. R. Kirtley, C. C. Chi, L. S. Yu-Jahnes, A. Gupta, T. Shaw, J. Z. Sun, and M. B. Ketchen, *Pairing Symmetry and Flux Quantization in a Tricrystal Superconducting Ring of YBa $2$ Cu $3$ O $7-\delta$* , *Phys. Rev. Lett.* **73**, 593 (1994).

- [9] A. V. Balatsky, I. Vekhter, and J.-X. Zhu, *Impurity-induced states in conventional and unconventional superconductors*, Rev. Mod. Phys. **78**, 373 (2006).
- [10] T. J. Reber, N. C. Plumb, Y. Cao, Z. Sun, Q. Wang, K. McElroy, H. Iwasawa, M. Arita, J. S. Wen, Z. J. Xu, G. Gu, Y. Yoshida, H. Eisaki, Y. Aiura, and D. S. Dessau, *Preparing and the “filling” gap in the cuprates from the tomographic density of states*, Phys. Rev. B **87**, 060506 (2013).
- [11] T. J. Reber, N. C. Plumb, Z. Sun, Y. Cao, Q. Wang, K. McElroy, H. Iwasawa, M. Arita, J. S. Wen, Z. J. Xu, G. Gu, Y. Yoshida, H. Eisaki, Y. Aiura, and D. S. Dessau, *The origin and non-quasiparticle nature of Fermi arcs in  $\text{Bi}_2\text{Sr}_2\text{CaCu}_2\text{O}_{8+\delta}$* , Nature Physics **8**, 606 (2012).
- [12] N. N. Bogoljubov, *On a new method in the theory of superconductivity*, II Nuovo Cimento (1955-1965) **7**, 794 (1958).
- [13] M. Tinkham, *Introduction to Superconductivity*, Dover Publications, 2 edition, 2004.
- [14] Y. He, Y. Yin, M. Zech, A. Soumyanarayanan, M. M. Yee, T. Williams, M. C. Boyer, K. Chatterjee, W. D. Wise, I. Zeljkovic, T. Kondo, T. Takeuchi, H. Ikuta, P. Mistark, R. S. Markiewicz, A. Bansil, S. Sachdev, E. W. Hudson, and J. E. Hoffman, *Fermi Surface and Pseudogap Evolution in a Cuprate Superconductor*, Science **344**, 608 (2014).
- [15] X. Li, C. Zou, Y. Ding, H. Yan, S. Ye, H. Li, Z. Hao, L. Zhao, X. Zhou, and Y. Wang, *Evolution of Charge and Pair Density Modulations in Overdoped  $\text{Bi}_2\text{Sr}_2\text{CuO}_{6+\delta}$* , Physical Review X **11**, 11007 (2021).
- [16] L. Capriotti, D. J. Scalapino, and R. D. Sedgewick, *Wave-vector power spectrum of the local tunneling density of states: Ripples in a  $d$ -wave sea*, Phys. Rev. B **68**, 014508 (2003).
- [17] D. Zhang and C. S. Ting, *Energy-dependent modulations in the local density of states of the cuprate superconductors*, Phys. Rev. B **67**, 100506 (2003).
- [18] N. E. Hussey, *Low-energy quasiparticles in high-  $T_c$  cuprates*, Advances in Physics **51**, 1685 (2002).
- [19] R. Joynt, *Bound states and impurity averaging in unconventional superconductors*, Journal of Low Temperature Physics **109**, 811 (1997).

- 
- [20] Zhou Wang, A. C. Bovik, H. R. Sheikh, and E. P. Simoncelli, *Image quality assessment: from error visibility to structural similarity*, IEEE Transactions on Image Processing **13**, 600 (2004).
- [21] P. Choubey, A. Kreisel, T. Berlijn, B. M. Andersen, and P. J. Hirschfeld, *Universality of scanning tunneling microscopy in cuprate superconductors*, Phys. Rev. B **96**, 174523 (2017).
- [22] A. Kreisel, P. Choubey, T. Berlijn, W. Ku, B. M. Andersen, and P. J. Hirschfeld, *Interpretation of Scanning Tunneling Quasiparticle Interference and Impurity States in Cuprates*, Phys. Rev. Lett. **114**, 217002 (2015).



# Appendices



## Comparing images using the SSIM

Comparing images is quite hard for computers. The reason being that most algorithms compare images pixel by pixel. For images containing more structured data, such an approach does not yield satisfactory results. By using the SSIM this problem is allayed [20]. The improvement is obtained by using three independent measures for comparison. The luminance, contrast and structure. The equation used to calculate the SSIM is given by

$$SSIM(x, y) = \frac{(2\mu_x\mu_y + C_1)(2\sigma_{xy} + C_2)}{(\mu^2 + \mu^2 + C_1)(\sigma_x^2 + \sigma_y^2 + C_2)} \quad (A.1)$$

Here  $x$  and  $y$  are the input images. The luminance  $\mu_x$  and contrast  $\sigma_x$  are respectively given by

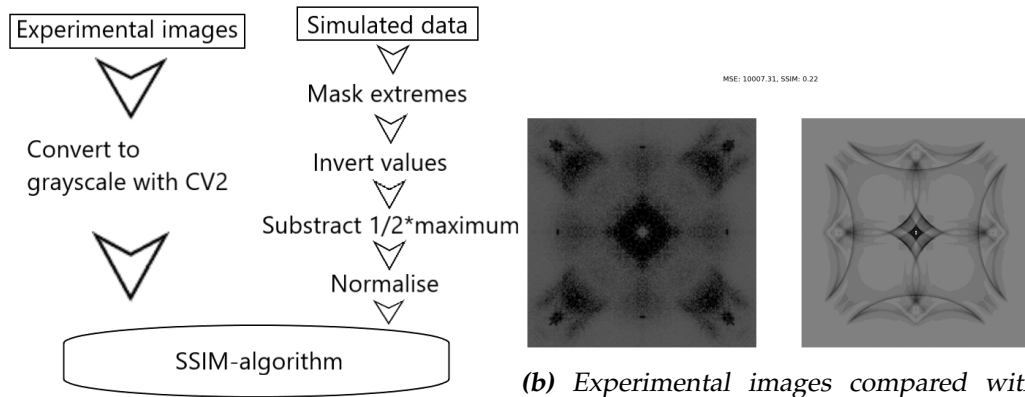
$$\mu_x = \frac{1}{N} \sum_{i=1}^N x_i \quad (A.2)$$

$$\sigma_x = \sqrt{\frac{1}{N-1} \sum_{i=1}^N (x_i - \mu_x)^2} \quad (A.3)$$

$$(A.4)$$

So the luminance is given by the mean of the intensity of an image, and the contrast as the deviation from this mean. Finally, for the structure coefficient we have

$$\sigma_{xy} = \frac{1}{N-1} \sum_{i=1}^N (x_i - \mu_x)(y_i - \mu_y) \quad (A.5)$$



**(b)** Experimental images compared with processed QPI simulations.

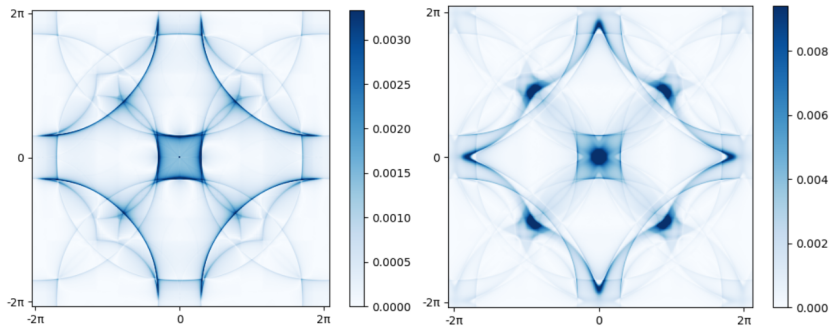
**(a)** The steps taken to make the data ready to be fed into the SSIM algorithm

The structure coefficient can be roughly interpreted as an innerproduct between the images after the luminance has been subtracted. The SSIM is then a product of these factors. As was the goal, comparison is not simply pixel by pixel. For the algorithm to produce sensible results additionally some image manipulation was necessary. Firstly all images had to be converted to greyscale. This means that all pixels should have values between -1 and 1. The experimental images were converted using CV2. For the generated QPI-patterns manual conversion was necessary. The procedure is shown in Fig. A.1a. First the extremes of the simulation are removed. Generally the simulation has a few extreme pixels in the center. Removing these is essential to avoid all other pixels to become zero when normalising. Next the values were inverted. The SSIM considers high values to be zero signal and vice versa. Then, to get into the appropriate range  $\frac{1}{2}$  of the maximum was subtracted. Lastly the values were normalised and the size of the simulation was adjusted to the size of the image.

# Appendix B

## Images for mentioned parameters

In this section we digress on some minor variations that occur for different parameters. First we have the images with the gap set to zero. As mentioned in the text, this is rather unphysical around the gap, but might be useful far above or below it. The most important observation is that the electron simulation in Fig. B.1a has no peaks at the corners between the arcs. The electron-hole simulation does have these peaks, and therefore looks more like the experimental image. This difference is obviously reduced when the gap is non-zero. Secondly we show the van Hove sin-



(a) The electron QPI pattern with gap set to zero.

(b) The electron and hole QPI pattern with gap set to zero.

**Figure B.1:** Simulations for different bands with the gap set to zero.

gularity above the Fermi energy at 30 meV. This singularity can be both due to the flipping of the quasi-particle dispersion relation or due to the scattering of electrons into empty hole states. Do note that compared to Fig. 4.4c the signal is slightly weaker. As can be seen in the experimental data in Fig. B.2a this should be the case.

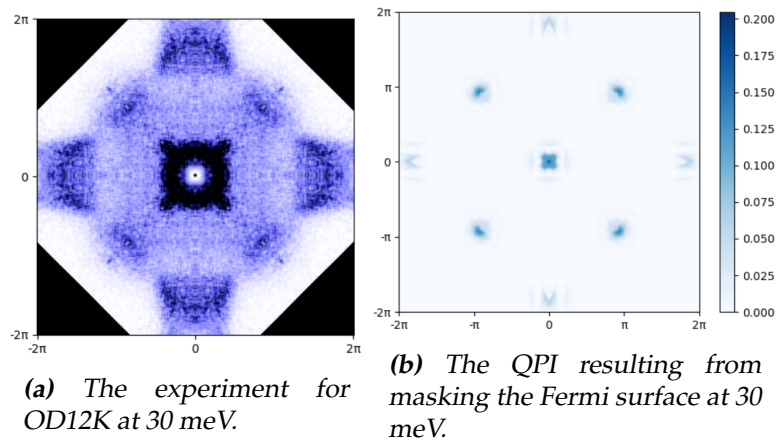


**Figure B.2:** The comparison for the van Hove singularity at +30 meV, so above the Fermi energy.